Floquet engineering ultracold polar molecules to simulate topological insulators

Thomas Schuster,[1] Felix Flicker,[1,2] Ming Li,[3] Svetlana Kotochigova,[3] Joel E. Moore,[1,4]
Jun Ye,[5] and Norman Y. Yao[1,4]

[1]*Department of Physics, University of California, Berkeley, California 94720, USA*
[2]*Rudolph Peierls Centre for Theoretical Physics, University of Oxford, Department of Physics, Clarendon Laboratory,*
Parks Road, Oxford OX1 3PU, United Kingdom
[3]*Department of Physics, Temple University, Philadelphia, Pennsylvania 19122, USA*
[4]*Materials Science Division, Lawrence Berkeley National Laboratory, Berkeley, California 94720, USA*
[5]*JILA, National Institute of Standards and Technology and Department of Physics, University of Colorado, Boulder, Colorado 80309, USA*

We present a quantitative, near-term experimental blueprint for the quantum simulation of topological insulators using lattice-trapped ultracold polar molecules. In particular, we focus on the so-called Hopf insulator, which represents a three-dimensional topological state of matter existing outside the conventional tenfold way and crystalline-symmetry-based classifications of topological insulators. Its topology is protected by a *linking number* invariant, which necessitates long-range spin-orbit-coupled hoppings for its realization. While these ingredients have so far precluded its realization in solid-state systems and other quantum simulation architectures, in an accompanying Letter [T. Schuster *et al.*, Phys. Rev. Lett. **127**, 015301 (2021)], we predict that Hopf insulators can arise naturally from the dipolar interaction. Here, we investigate a specific polar molecule architecture, where the effective "spin" is formed from sublattice degrees of freedom. We introduce two techniques that allow one to optimize dipolar Hopf insulators with large band gaps, and which should also be readily applicable to the simulation of other exotic band structures. First, we describe the use of Floquet engineering to control the range and functional form of dipolar hoppings and, second, we demonstrate that molecular AC polarizabilities (under circularly polarized light) can be used to precisely tune the resonance condition between different rotational states. To verify that this latter technique is amenable to current-generation experiments, we calculate, from first principles, the AC polarizability for σ^+ light for $^{40}K\,^{87}Rb$. Finally, we show that experiments are capable of detecting the unconventional topology of the Hopf insulator by varying the termination of the lattice at its edges, which gives rise to three distinct classes of edge mode spectra.

I. INTRODUCTION

The rich internal structure of ultracold polar molecules has led to intense interest for their use in a wide range of applications, ranging from quantum simulation and computation to ultracold chemistry and precision measurement [1–16]. Understanding and controlling this structure has led to the development of a host of techniques enabling the preparation and manipulation of rovibrational states in polar molecules [16–25]. From the perspective of quantum simulation, polar molecules enjoy a unique advantage compared to their neutral atom cousins, owing to the presence of strong, anisotropic, long-range dipolar interactions; these interactions have proven useful for theoretical proposals aiming to realize a number of exotic phases, including disordered quantum magnets [26–28], Weyl semimetals [29], and fractional Chern insulators [28,30]. Motivated, in part, by these prospects, the last decade has seen tremendous experimental progress, advancing from rovibrational ground-state cooling [16] to the recent realization of a Fermi degenerate molecular gas [24]. Moreover, from a geometric perspective, molecules can either be loaded into optical lattices [22] or optical tweezer arrays [25]. As in other quantum simulation

platforms, Floquet engineering [31,32]—high-frequency, periodic time modulation—can further sculpt the molecules' interaction, broadening the scope of accessible phases [33,34].

In this article, we provide an explicit experimental blueprint for realizing another unobserved phase of matter, the Hopf insulator, in polar molecules. The Hopf insulator is a particular topological insulator, characterized by a *linking number* topological invariant arising from the unique topology of knots in three dimensions and the Hopf map of mathematics [35,36]. Notably, it exists only in two-band systems, falling outside the traditional "tenfold way" classification of topological insulators [37,38] and suggesting that it might possess different physics than the most well-known examples of these phases. Despite much interest in both the Hopf insulator [36,39–50] and the physics associated with the Hopf map more generally [51–54], experimentally realizing the Hopf insulator has remained an open challenge, and even proposed implementation platforms (e.g., in either conventional quantum materials or cold atomic quantum simulators) remain few and far between [41,45]. The key challenges arise directly from the nature of the Hopf map. In particular, realizing the Hopf insulator requires two essential ingredients: (1) the presence of long-range hoppings and (2) strong spin-orbit

coupling, manifested in hoppings whose phase is spatially anisotropic.

In an accompanying Letter [55], we predict that combining the dipolar interaction with Floquet engineering [31,32] can naturally give rise to the Hopf insulator in interacting spin systems. Here, we build upon this result by providing a quantitative blueprint using lattice-trapped ultracold polar molecules, focusing for concreteness on ^{40}K ^{87}Rb [16,18–22]. Our approach takes advantage of the full tool set of controls developed for polar molecular systems. In particular, we envision a deep, three-dimensional optical lattice, so that the molecules' rotational motion constitutes the fundamental degrees of freedom in the system. Rotational excitations are exchanged between lattice sites via the dipolar interaction, which simulates the hopping of hard-core bosons on the lattice. The two-band, or "spin," degrees of freedom of the Hopf insulator are formed from two sublattices, distinguished from each other by the lattice light itself—different intensity light forming the two sublattices induces different level structures in the trapped molecules, according to the molecules' polarizability [23].

In contrast to prior studies [28,30,56], we utilize this polarizability to isolate the $\Delta m = \pm 1$ angular-momentum-changing component of the dipolar interaction, which *precisely* induces the requisite spin-orbit coupling of the Hopf insulator [36]. To complete our construction, we demonstrate that Floquet engineering can be implemented using amplitudes of applied laser light and DC electric fields, which are easily accessible in current-generation experiments; moreover, we show that this engineering can tune the system's hoppings into the Hopf insulating phase with large band gaps $\gtrsim 0.26 t_{nn}$ (in units of the nearest-neighbor hopping, t_{nn}), enabling easier experimental observation. Finally, a particularly simple way to achieve the requisite rotational level structure (Fig. 1) is to utilize circularly polarized optical radiation in conjunction with the molecule's AC polarizability. To this end, in order to demonstrate quantitative feasibility, we provide detailed calculations of the relevant circular polarizabilities for ^{40}K ^{87}Rb.

Direct experimental verification of the Hopf insulator is most simply achieved through spectroscopy of its gapless edge modes. In the accompanying Letter [55], we demonstrate that these edge modes are robust at any smooth boundary of the Hopf insulating phase, while for sharp boundaries, their presence or absence signifies the existence of an underlying crystalline symmetry [44]. We will show that all three of these qualitatively distinct boundary spectra can be manufactured and probed in ultracold polar molecule simulations. Since the Hopf insulator's edge behavior is a direct result of it being outside the conventional tenfold way, this serves as a direct experimental probe of the Hopf insulator's unique topological classification.

Our manuscript is structured as follows. We begin with an overview of the Hopf insulator, with a specific focus on the requirements—a two-band system, and long-range, spin-orbit-coupled hoppings. We then turn to the setting of our proposal, outlining precisely how the rotational excitations of polar molecules can simulate spin-orbit-coupled particles hopping on a lattice. Next, we demonstrate how particular patterns of Floquet driving can provide tremendous control
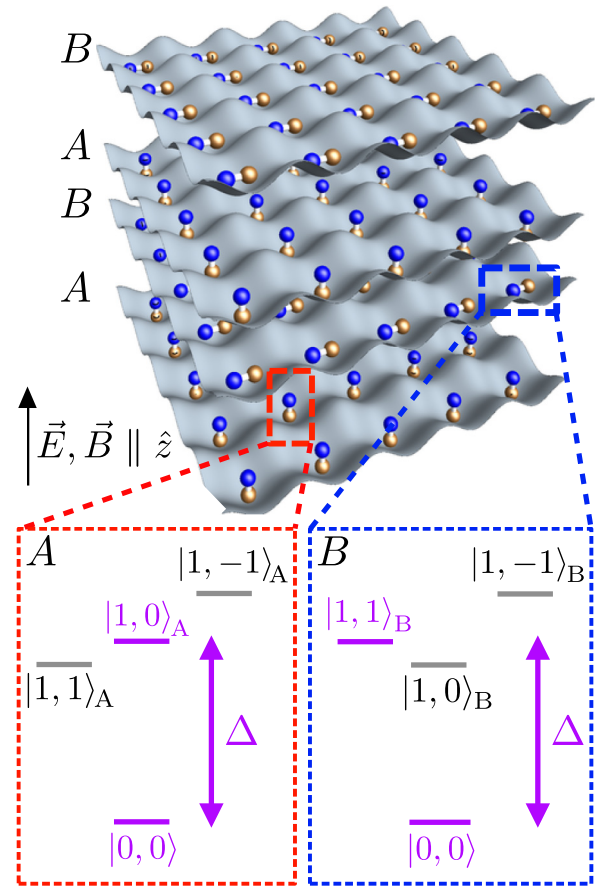

FIG. 1. Schematic geometry depicting a three-dimensional (3D) optical lattice of polar molecules with two layered sublattices A and B. Orbital motion of the molecules is frozen by the optical lattice. The level structure of the $J = 0, 1$ rotational states on the A (left) and B (right) sublattices. The purple highlighted states form the hard-core bosonic doublet for each sublattice, and their energy splitting Δ is tuned by external fields to be degenerate between sublattices.

over these hoppings, and numerically verify that these can be used to tune the system into a large band-gap, Hopf insulator phase. We present the edge modes of the polar molecular Hopf Hamiltonian and show that they display three qualitatively distinct spectra, dependent on the lattice termination. Finally, we conclude by providing a detailed description of all aspects of the proposal's implementation in a three-dimensional optical lattice of ^{40}K ^{87}Rb.

II. THE HOPF INSULATOR

We begin with an introduction to the Hopf insulator, seeking to motivate the connection between the linking number interpretation of the Hopf invariant and the long-range spin-orbit coupling required for its physical realization.

The Hopf insulator is a particular type of topological insulator [57–64], a class of phases of matter most notable for exhibiting conducting surface states despite an insulating bulk. They are differentiated from conventional insulators by a nonzero topological invariant associated with their underlying spin-orbit-coupled band structure; moreover, their surface states are unusually robust to the detrimental effects of

impurities. Their organization was first captured via the so-called tenfold way classification [37,38], and consists of a wide landscape of phases dependent on a system's dimensionality and symmetries. Nevertheless, more recent work has exposed topological insulators that exist beyond this classification framework; notable examples include topological crystalline insulators [65], higher-order topological insulators [66], and our insulator of interest, the Hopf insulator [36,39–41,43–45].

The Hopf insulator exists in three dimensions in the *absence* of any symmetries, for which the tenfold way classification [37,38] would nominally predict only an ordinary insulator. In our context, it will consist of hard-core boson degrees of freedom hopping on a three-dimensional lattice (although one is accustomed to thinking of topological insulators in terms of fermions, their single-particle nature also enables a hard-core bosonic realization). The bosons come in two "pseudospins," A and B, which will form the two bands of the system. These may be formed from physical spins, but are not required to be—in our realization, they will correspond to two sublattices of the three-dimensional lattice. In real space, the Hopf insulator Hamiltonian takes the generic form

$$H_{\text{eff}} = \frac{1}{2} \sum_{\substack{\mathbf{v}, \mathbf{r} \neq \mathbf{0}, \\ \alpha, \beta}} \left[t_{\mathbf{r}}^{\alpha\beta} a_{\mathbf{v}+\mathbf{r},\alpha}^{\dagger} a_{\mathbf{v},\beta} + \text{H.c.} \right] + \sum_{\mathbf{v},\alpha} \mu^{\alpha} a_{\mathbf{v},\alpha}^{\dagger} a_{\mathbf{v},\alpha}, \quad (1)$$

where $a_{\mathbf{v},\alpha}^{\dagger}$ is the creation operator for a hard-core boson at lattice site $\mathbf{v}$ of pseudospin $\alpha \in \{A, B\}$. The Hamiltonian consists of both pseudospin-preserving ($t_{\mathbf{r}}^{AA}$ and $t_{\mathbf{r}}^{BB}$) and pseudospin-flipping ($t_{\mathbf{r}}^{AB}$ and $t_{\mathbf{r}}^{BA}$) hoppings, as well as a pseudospin-dependent chemical potential μ^{α}.

The topology of the Hopf insulator is most easily seen in its momentum-space representation, governed by the two-by-two matrix $H^{\alpha\beta}(\mathbf{k}) = \sum_{\mathbf{r}} \tilde{t}_{\mathbf{r}}^{\alpha\beta} e^{i\mathbf{k}\cdot\mathbf{r}} + \mu^{\alpha}\delta^{\alpha\beta}$. This is conveniently decomposed as $H(\mathbf{k}) = n_0(\mathbf{k})\mathbb{1} + \mathbf{n}(\mathbf{k}) \cdot \boldsymbol{\sigma}$, where the Pauli matrices $\boldsymbol{\sigma}$ act on the pseudospin degrees of freedom, which form the two bands of the Hopf insulator, and the condition that the bands are gapped requires $|\mathbf{n}(\mathbf{k})| > 0$. We can view this Hamiltonian as a map that takes vectors $\mathbf{k}$ in the Brillouin zone to points $\hat{\mathbf{n}} \equiv \mathbf{n}/|\mathbf{n}|$ on the Bloch sphere. To see the Hopf insulator's topology, consider the *pre-images* of two different Bloch sphere points $\hat{\mathbf{n}}$, $\hat{\mathbf{n}}'$ in the Brillouin zone, i.e., the set of momenta $\mathbf{k}$ such that $\hat{\mathbf{n}}(\mathbf{k}) = \hat{\mathbf{n}}$, or $\hat{\mathbf{n}}(\mathbf{k}) = \hat{\mathbf{n}}'$. Since the Brillouin zone is three dimensional—one dimension higher than the Bloch sphere—these pre-images are generically 1D loops in the Brillouin zone. The Hopf invariant h of the Hamiltonian $H(\mathbf{k})$ is precisely equal to the *linking number* of these two loops, for any choice of $\hat{\mathbf{n}}$, $\hat{\mathbf{n}}'$ [Fig. 2(a)]. The invariant can be calculated from the Bloch Hamiltonian via the Chern-Simons form [36],

$$h = \int_{\text{BZ}} d^3\mathbf{k} \; j^{\mu}(\mathbf{k}) A_{\mu}(\mathbf{k}), \quad (2)$$

where $j^{\mu}(\mathbf{k}) = \frac{1}{8\pi} \epsilon^{\mu\nu\lambda} \hat{\mathbf{n}} \cdot (\partial_{k_{\nu}} \hat{\mathbf{n}} \times \partial_{k_{\lambda}} \hat{\mathbf{n}})$ is the Berry curvature and $A_{\mu}(\mathbf{k})$ its associated vector potential.

The linking number interpretation leads to two observations, one which explains the need for long-range hoppings and the other which justifies the required form of spin-orbit coupling. First, the rapid variation in $\mathbf{n}(\mathbf{k})$ required
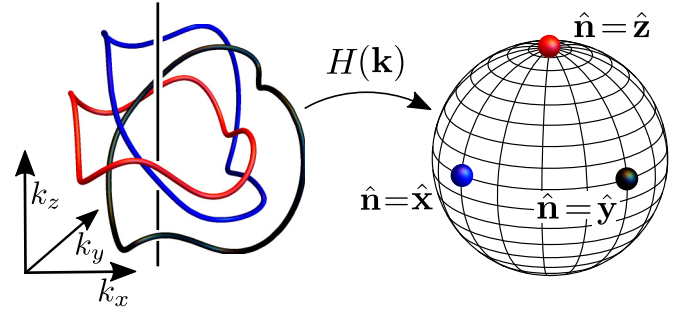

FIG. 2. The Hamiltonian of the Hopf insulator maps closed loops in the Brillouin zone to points on the Bloch sphere, with the unique property that any two loops have linking number equal to the Hopf invariant. The above loops are solved for using the proposed experimental dipolar spin Hamiltonian specified in the text—their linking provides a visual verification of the Hopf insulating phase. The $\hat{\mathbf{n}} = \hat{\mathbf{x}}, \hat{\mathbf{y}}$ pre-images (blue, black tubes) are $90°$ rotations of each other about the k_z axis (vertical black line) due to the spin-orbit-coupled hopping $t_{\mathbf{r}}^{AB} \sim e^{i\phi}$.

for pre-image linking necessitates the presence of strong long-range hoppings, which contribute oscillations $\sim e^{i\mathbf{k}\cdot\mathbf{r}}$ to $\mathbf{n}(\mathbf{k})$, at a frequency proportional to their range $\mathbf{r}$. Specifically, no nearest-neighbor Hamiltonian is known for the Hopf insulator; the prototypical Hopf insulator Hamiltonian [36] features as far as next-next-nearest-neighbor hoppings. Second, pre-image linking, by definition, requires a strong coupling between the pseudospin degree of freedom and the momentum, much as is true for other topological insulators. Inspired by the model of Ref. [36], in this work we realize a specific form of this spin-orbit coupling, generated via pseudospin-flipping hoppings with a direction-dependent phase $t_{\mathbf{r}}^{AB} \sim e^{i\phi}$, where ϕ is the azimuthal angle of the hopping displacement $\mathbf{r}$ (Fig. 3). This form of hopping locks the n_x, n_y components of the pseudospin to the k_x, k_y components of the momentum, such that the pre-image of, e.g., $\hat{\mathbf{n}} = \hat{\mathbf{x}}$, is exactly a 90 degree rotation about the k_z axis of the pre-image of $\hat{\mathbf{n}} = \hat{\mathbf{y}}$. As illustrated in Fig. 2, this simple correspondence
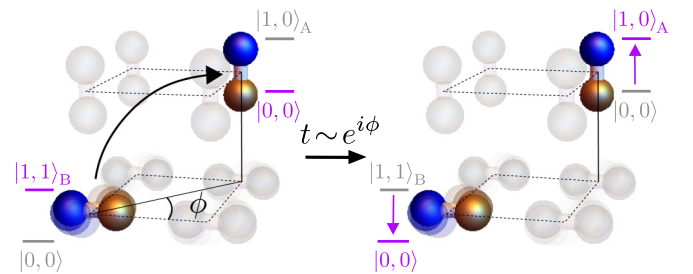

FIG. 3. Depiction of the intersublattice "hopping" $|0,0\rangle_A |1,1\rangle_B \rightarrow |1,0\rangle_A |0,0\rangle_B$, in which a hard-core bosonic excitation on sublattice B hops to sublattice A. This is induced by the dipolar interaction, and occurs with a hopping matrix element $t_{\mathbf{r}}^{AB} \sim e^{i\phi}$ with phase equal to the azimuthal angle ϕ between the dipoles. This phase profile arises from the spherical harmonic $C_{-\Delta m=1}^{2}(\theta, \phi)$, since the hopping changes the total angular momentum of the system by $\Delta m = -1$. Sublattice B molecules are depicted as spinning to indicate their nonzero z-angular momentum in the excited state.

leads naturally to linking of the two pre-images. While this simple argument applies only to pre-images related by 90 or 180 degree rotations about the z axis (due to the cubic lattice symmetry), this is, in fact, sufficient: in a gapped model, the linking number is *constant* for all pairs of pre-images. We note that this same phase profile of the hoppings is also present in two-dimensional realizations of Chern insulating physics, both in the prototypical Qi-Wu-Zhang model [67] as well as in positionally disordered systems [68].

In the following two sections, we demonstrate that systems of dipolar interacting spins provide a natural ground to realize both of these key ingredients. We begin by describing how a particular configuration of the spins' level structures leads to the effective hard-core boson Hamiltonian of Eq. (1), including the desired spin-orbit coupling $t_{\mathbf{r}}^{AB} \sim e^{i\phi}$. We then augment the bare dipolar hoppings with a Floquet engineering scheme, which serves to decrease the relative strength of nearest-neighbor hoppings and provides useful experimental parameters for tuning into the Hopf insulating phase.

III. THE DIPOLAR HAMILTONIAN

We now turn to the setting of our proposal. We envision a three-dimensional optical lattice filled with ultracold polar molecules. We work in the deep lattice limit, so that the molecules themselves do not hop between lattice sites, and the molecules' rotational states form the fundamental degrees of freedom of our system [21]. As shown in Fig. 1, the lattice is formed by alternating planes of two-dimensional square lattices, stacked in the z direction. These form two sublattices, A and B, which will play the role of the pseudospin in the Hopf insulator.

The molecules are most strongly governed by the rotational Hamiltonian $H_{\text{rot}} = \Delta \mathbf{J}^2$, with eigenstates $|J, m_J\rangle$ indexed by their orbital (J) and magnetic (m_J) angular momentum quantum numbers, which have energies $E = \Delta J(J+1)$ and wave functions described by the spherical harmonic functions [69]. While naturally organized into degenerate manifolds of each J, the m_J eigenstates are split by both intrinsic hyperfine interactions and *tunable* extrinsic effects resulting from electric fields, magnetic fields, and incident laser light. These extrinsic effects (which set the molecules' quantization axis, i.e., $\hat{\mathbf{z}}$ in Fig. 1) enable a direct modulation of the rotational states' energies in both *space* (to distinguish between the A and B sublattices) and *time* (to implement Floquet engineering).

We now aim to use these rotational states to realize an effective Hamiltonian of hard-core bosons, as in Eq. (1). We focus on the lowest four rotational eigenstates (i.e., the $J = 0, 1$ manifolds), and use these to define two distinct hard-core bosonic degrees of freedom. On the A sublattice, we form a hard-core boson from the doublet $\{|0_A\rangle = |0, 0\rangle_A, |1_A\rangle = |1, 0\rangle_A\}$, while on the B sublattice, we utilize $\{|0_B\rangle = |0, 0\rangle_B, |1_B\rangle = |1, 1\rangle_B\}$, as illustrated in Fig. 1. The hard-core bosons interact with each other through the dipolar interaction [70],

$$H_{\text{dd}}^{ij} = \frac{-\sqrt{6}}{4\pi\epsilon_0 r^3} \sum_{\Delta m_J = -2}^{2} C_{-\Delta m_J}^2(\theta, \phi) T_{\Delta m_J}^2(\mathbf{d}^{(i)}, \mathbf{d}^{(j)}), \quad (3)$$

where (r, θ, ϕ) parameterizes the separation of the interacting molecules i and j in spherical coordinates, and we compress the unit and sublattice indices into a single index $i = \mathbf{v}, \alpha$. The dipole moment operator $\mathbf{d}^{(i)} = (d_-^{(i)}, d_z^{(i)} d_+^{(i)})$ is a rank-1 spherical tensor acting on the rotational states of the molecule i, whose three components change the molecule's magnetic quantum number by $(-1, 0, +1)$, respectively. The spherical harmonics $C_{-\Delta m}^2(\theta, \phi)$ capture the spatial dependence of the interaction and are accompanied by the corresponding component of $T_{\Delta m}^2$, the unique rank-2 spherical tensor generated from the dipole operators $\mathbf{d}^{(i)}$, $\mathbf{d}^{(j)}$. Explicitly, we have $T_{\pm 2}^2 = d_\pm^{(i)} d_\pm^{(j)}$, $T_{\pm 1}^2 = (d_\pm^{(i)} d_z^{(j)} + d_z^{(i)} d_\pm^{(j)})/\sqrt{2}$, $T_0^2 = (d_\pm^{(i)} d_\mp^{(j)} + 2 d_z^{(i)} d_z^{(j)} + d_\mp^{(i)} d_\pm^{(j)})/\sqrt{6}$.

A few remarks are in order. First, we will assume that the dipolar interaction strength is significantly weaker than the energy splittings within the $J = 1$ manifold. Second, we will tune the splitting between the $|0_A\rangle$ and $|1_A\rangle$ states to be resonant with that of the $|0_B\rangle$ and $|1_B\rangle$ states (Fig. 1). Conservation of energy then dictates that the dipolar interaction can only induce transitions within our prescribed hard-core bosonic doublets, i.e., those that preserve boson number. These transitions take the form of hoppings in the bosonic Hamiltonian, $t_{ij} = \langle 0_i, 1_j | H_{\text{dd}}^{ij} | 1_i, 0_j \rangle$.

These hoppings may occur either within a sublattice ($t_{\mathbf{r}}^{AA}$ and $t_{\mathbf{r}}^{BB}$) or across sublattices ($t_{\mathbf{r}}^{AB}$). With the prescribed geometry and level structure, we have

$$t_{\mathbf{r}}^{AA} = -\frac{d_{00}^2}{4\pi\epsilon_0} \frac{3\cos^2(\theta) - 1}{r^3},$$

$$t_{\mathbf{r}}^{BB} = \frac{d_{01}^2}{8\pi\epsilon_0} \frac{3\cos^2(\theta) - 1}{r^3}, \quad (4)$$

$$t_{\mathbf{r}}^{AB} = \left(t_{-\mathbf{r}}^{BA}\right)^* = -\frac{3\, d_{00} d_{01}}{4\sqrt{2}\pi\epsilon_0} \frac{\cos(\theta)\sin(\theta)}{r^3} e^{i\phi},$$

where (r, θ, ϕ) parameterizes the displacement between sites in spherical coordinates, equal to $\mathbf{r}$ for intrasublattice hoppings and $\mathbf{r} + b\hat{\mathbf{z}}$ for intersublattice hoppings (where b is the vertical distance between A and B planes), and d_{00}, d_{01} are the dipole moments $d_{00} = \langle 1, 0 | d_z | 0, 0 \rangle$ and $d_{01} = \langle 1, \pm 1 | d_\pm | 0, 0 \rangle$. Our choice of rotational states guarantees that the intersublattice hopping $t_{\mathbf{r}}^{AB}$ arises solely from the $\Delta m_J = +1$ term in H_{dd}, which gives rise to a hopping phase $t_{\mathbf{r}}^{AB} \sim e^{i\phi}$ via the C_{-1}^2 spherical harmonic. As illustrated in Fig. 2, this naturally leads to linking between the Bloch sphere pre-images. Finally, variations in the energy splitting between sublattices naturally appear as effective chemical potentials μ^α, completing the realization of the Hamiltonian given by Eq. (1).

IV. FLOQUET ENGINEERING

While the dipolar interaction elegantly realizes the requisite spin-orbit coupling, relatively strong nearest-neighbor hopping as well as the slow asymptotic decay of the $1/R^3$ power law preclude numerical observation of the Hopf insulator. To this end, we utilize Floquet engineering to two effects: first, to decrease "odd" hoppings in the xy plane (those with odd $r_x + r_y$) and, second, to truncate the dipolar power law in the z direction [32]. We achieve each effect by

adding spatiotemporal dependence to the chemical potential $\mu_{\mathbf{v}}^{\alpha}(t)$, and oscillating each $\mu_{\mathbf{v}}^{\alpha}(t)$ at timescales much faster than the hopping. Under certain conditions (specified below), this leads to an effective time-*independent* Hamiltonian of the same form as Eq. (1), but with modified hoppings,

$$t_{\mathbf{r}}^{\alpha\beta} \rightarrow \beta_{\mathbf{r}}^{\alpha\beta}\, t_{\mathbf{r}}^{\alpha\beta}, \qquad (5)$$

where the damping coefficients $\beta_{\mathbf{r}}^{\alpha\beta}$ are determined by the specific profiles of the oscillated chemical potentials, $\mu_{\mathbf{v}}^{\alpha}(t)$. In what follows, we first derive this relation explicitly [Eq. (12)], and then introduce two Floquet engineering schemes [i.e., explicit profiles for the spatiotemporal dependence of $\mu_{\mathbf{v}}^{\alpha}(t)$] that achieve the hopping modifications described above.

A. Overview of Floquet engineering

We begin with a broad introduction to Floquet engineering using a time-dependent chemical potential, following Ref. [32] but modified to include sublattices and complex hoppings. We consider a time-dependent Hamiltonian of the form given by Eq. (1) where the chemical potential $\mu_{\mathbf{v}}^{\alpha}(t)$ now varies with the lattice site $\mathbf{v}$ as well as periodically in time t, with a period T. To calculate the effect of the driving, we move into a rotating frame, defining the unitary

$$U(t) = \exp\left[-i \int_0^t dt'\, \frac{1}{2} \sum_{\mathbf{v},\alpha} \mu_{\mathbf{v}}^{\alpha}(t') \sigma_{\mathbf{r}}^z \right], \qquad (6)$$

and the rotated wave function

$$|\Psi'(t)\rangle = U^{\dagger}(t)|\Psi(t)\rangle, \qquad (7)$$

whose time evolution is governed by the Hamiltonian

$$
\begin{aligned}
H'(t) &= U^{\dagger}(t) H(t) U(t) - i U^{\dagger}(t) \dot{U}(t) \\
&= \frac{1}{2} \sum_{\substack{\mathbf{v},\, \mathbf{r} \neq \mathbf{0}, \\ \alpha,\, \beta}} \left(\exp\left\{ -i \int_0^t dt'\, [\mu_{\mathbf{v}+\mathbf{r}}^{\alpha}(t') - \mu_{\mathbf{v}}^{\beta}(t')] \right\} \right. \\
&\quad \left. \times t_{\mathbf{r}}^{\alpha\beta}\, a_{\mathbf{v}+\mathbf{r},\alpha}^{\dagger} a_{\mathbf{v},\beta} + \text{H.c.} \right).
\end{aligned}
\qquad (8)
$$

At high frequencies, $1/T \gg |t_{\mathbf{r}}^{\alpha\beta}|$, the rotated Hamiltonian is well approximated by replacing all quantities by their average over a single period. This gives an effective time-independent Hamiltonian

$$
\begin{aligned}
H^{\text{eff}} &= \frac{1}{2} \sum_{\substack{\mathbf{v},\, \mathbf{r} \neq \mathbf{0}, \\ \alpha,\, \beta}} \left[\beta_{\mathbf{v}+\mathbf{r},\mathbf{v}}^{\alpha\beta}\, t_{\mathbf{r}}^{\alpha\beta}\, a_{\mathbf{v}+\mathbf{r},\alpha}^{\dagger} a_{\mathbf{v},\beta} + \text{H.c.} \right] \\
&\quad + \sum_{\mathbf{v},\alpha} \mu_{\mathbf{v}}^{\alpha}\, a_{\mathbf{v},\alpha}^{\dagger} a_{\mathbf{v},\alpha},
\end{aligned}
\qquad (9)
$$

with a static chemical potential

$$\mu_{\mathbf{v}}^{\alpha} = \frac{1}{T} \int_0^T dt\, \mu_{\mathbf{v}}^{\alpha}(t), \qquad (10)$$

and hoppings suppressed by the dampings,

$$
\begin{aligned}
\beta_{\mathbf{v}+\mathbf{r},\mathbf{v}}^{\alpha\beta} &= \frac{1}{T} \int_0^T dt\, \exp\left\{ -i \int_0^t dt'\, [\mu_{\mathbf{v}+\mathbf{r}}^{\alpha}(t') - \mu_{\mathbf{v}}^{\beta}(t')] \right\} \\
&= \frac{1}{T} \int_0^T dt\, \left(\cos\left\{ \int_0^t dt'\, [\mu_{\mathbf{v}+\mathbf{r}}^{\alpha}(t') - \mu_{\mathbf{v}}^{\beta}(t')] \right\} \right. \\
&\quad \left. - i \sin\left\{ \int_0^t dt'\, [\mu_{\mathbf{v}+\mathbf{r}}^{\alpha}(t') - \mu_{\mathbf{v}}^{\beta}(t')] \right\} \right).
\end{aligned}
\qquad (11)
$$

For convenience, we will always choose $\mu_{\mathbf{v}}^{\alpha}(t)$ to be an even function of t, in which case the imaginary part of the damping vanishes and we have

$$\beta_{\mathbf{v}+\mathbf{r},\mathbf{v}}^{\alpha\beta} = \frac{1}{T} \int_0^T dt\, \cos\left\{ \int_0^t dt'\, [\mu_{\mathbf{v}+\mathbf{r}}^{\alpha}(t') - \mu_{\mathbf{v}}^{\beta}(t')] \right\}. \qquad (12)$$

In this case, the dampings modulate only the hoppings' magnitudes, and not their phase.

Since the modulation is generically inhomogeneous, care must be taken to ensure that the dampings are in fact translation invariant, $\beta_{\mathbf{v}+\mathbf{r},\mathbf{v}}^{\alpha\beta} = \beta_{\mathbf{r}}^{\alpha\beta}$, if one desires translation invariance in the effective Hamiltonian. This constraint requires that $\cos\{\int_0^t dt'\, [\mu_{\mathbf{v}+\mathbf{r}}^{\alpha}(t') - \mu_{\mathbf{v}}^{\alpha}(t')]\}$ be independent of $\mathbf{v}$. For intrasublattice hoppings ($\alpha = \beta$), there are two ways to achieve this: (1) with a "gradient" modulation, where $\mu_{\mathbf{v}}^{\alpha}(t)$ is linear in $\mathbf{v}$, and (2) with an "even-odd" modulation $\mu_{\mathbf{v}}^{\alpha}(t) = \mu^{\alpha}(-1)^{s_x v_x + s_y v_y + s_z v_z}$, $s_i \in \{0, 1\}$. (The latter is possible because we restrict to the cosine term of Eq. (11), which is even in μ and thus requires only the absolute value of $\mu_{\mathbf{v}+\mathbf{r}}^{\alpha}(t') - \mu_{\mathbf{v}}^{\alpha}(t')$ to be independent of $\mathbf{v}$.) For intersublattice hoppings ($\alpha \neq \beta$), this constraint additionally requires that the sublattices' modulations differ only by a *position-independent* function of time, namely,

$$\mu_{\mathbf{v}}^{A}(t) = \mu_{\mathbf{v}}(t), \qquad \mu_{\mathbf{v}}^{B}(t) = \mu_{\mathbf{v}}(t) + \mu_{\text{SL}}(t). \qquad (13)$$

These lead to damping coefficients,

$$
\begin{aligned}
\beta_{\mathbf{r}}^{AA} = \beta_{\mathbf{r}}^{BB} &= \frac{1}{T} \int_0^T dt\, \cos\left\{ \int_0^t dt'\, [\mu_{\mathbf{v}+\mathbf{r}}(t') - \mu_{\mathbf{v}}(t')] \right\}, \\
\beta_{\mathbf{r}}^{AB} &= \frac{1}{T} \int_0^T dt\, \cos\left\{ \int_0^t dt'\, [\mu_{\mathbf{v}+\mathbf{r}}(t') - \mu_{\mathbf{v}}(t') - \mu^{\text{SL}}(t')] \right\},
\end{aligned}
\qquad (14)
$$

for the intra- and intersublattice hoppings. We must also ensure that $\mu_{\mathbf{v}}^{\alpha}$ is translation invariant, which requires only that the average modulation is the same in each unit cell $\mathbf{v}$.

B. Even-odd modulation in *xy* plane

The first scheme for Floquet engineering serves to suppress the strength of nearest-neighbor hoppings relative to next-nearest-neighbor hoppings in the *xy* plane. The modulation takes the form of the even-odd modulation previously mentioned, with $s_x = s_y = 1$, $s_z = 0$. Specifically, we take

$$
\begin{aligned}
\mu_{\mathbf{v}}^{xy}(t) &= \tfrac{1}{2}(-1)^{v_x + v_y} \Omega^{xy} g^{xy} \cos(\Omega^{xy} t), \\
\mu_{\text{SL}}^{xy}(t) &= \Omega^{xy} g_{\text{SL}}^{xy} \cos(\Omega^{xy} t),
\end{aligned}
\qquad (15)
$$

where frequency Ω^{xy} is 2π times the inverse period, and g^{xy} and g_{SL}^{xy} are parameters to be tuned. Performing the integral inside Eq. (14) and using $\frac{1}{T} \int_0^T dt\, \cos[g \sin(2\pi t/T)] =$

$\frac{1}{2\pi}\int_0^{2\pi} dx \, \cos\left[g\sin(x)\right] = J_0(g)$ gives damping coefficients

$$\beta_{\mathbf{r}}^{xy,AA} = \begin{cases} J_0(g^{xy}), & r_x + r_y = \text{odd} \\ 1, & r_x + r_y = \text{even}, \end{cases}$$

$$\beta_{\mathbf{r}}^{xy,AB} = \begin{cases} J_0(g^{xy} + g_{SL}^{xy}), & r_x + r_y = \text{odd} \\ J_0(g_{SL}^{xy}), & r_x + r_y = \text{even}, \end{cases} \quad (16)$$

where $J_0(g)$ is a Bessel function of the first kind. We see that "odd" distance hoppings (including nearest neighbor, $r_x + r_y = 1$) are reduced relative to "even" hoppings (including next-nearest [$r_x = r_y = 1$] and next-next-nearest neighbor [$r_x = 2, r_y = 0$, and vice versa] hoppings, both with $r_x + r_y = 2$). The parameters g^{xy} and g_{SL}^{xy} give independent control over the ratio of even to odd hoppings for both inter- and intrasublattice hoppings.

C. Truncation in the *z* direction

The second use of Floquet modulation is to truncate hoppings from power law to short ranged in the z direction [32]. Unlike the previous xy modulation, we do not have an intuitive explanation for why one needs such a truncation. Nevertheless, we observe numerically that it is necessary for realizing the Hopf insulator phase. We take $\mu_{\mathbf{v}}^z(t)$ to be a gradient in the z direction,

$$\mu_{\mathbf{v}}^z(t) = v_z \Omega^z g^z(\Omega^z t), \quad \mu_{SL}^z(t) = \Omega^z g_{SL}^z(\Omega^z t), \quad (17)$$

with frequency Ω^z in time. This gives dampings

$$\beta_{\mathbf{r}}^{z,AA} = \frac{1}{2\pi}\int_0^{2\pi} dx \, \cos\left[r_z \int_0^x dx' \, g^z(x')\right],$$

$$\beta_{\mathbf{r}}^{z,AB} = \frac{1}{2\pi}\int_0^{2\pi} dx \, \cos\left\{\int_0^x dx' \left[r_z g^z(x') - g_{SL}^z(x')\right]\right\}. \quad (18)$$

These can be evaluated numerically once the functions $g^z(\Omega_z t)$, $g_{SL}^z(\Omega_z t)$ are chosen. Reference [32] showed that the modulation can be tuned to give hoppings that are effectively nearest neighbor in the z direction, at the cost of some loss of magnitude of the nearest-neighbor ($|r_z| = 1$) hopping. For experimental simplicity, we take the modulations to be piecewise constant in time,

$$\frac{\mu_{A,\mathbf{v}}^z(\Omega_z t)}{\Omega_z} = \begin{cases} (2g_1 + 2)v_z, & 0 < \Omega_z t \leqslant \phi_1/2 \\ (2g_2 + 2)v_z, & \phi_1 < \Omega_z t \leqslant \phi_2/2 \\ (2g_3 + 2)v_z, & \phi_2 < \Omega_z t \leqslant \pi/2 \\ -\mu_{A,\mathbf{v}}^z(\pi - \Omega_z t) + 4v_z, & \pi/2 < \Omega_z t \leqslant \pi \\ -\mu_{A,\mathbf{v}}^z(2\pi - \Omega_z t), & \pi < \Omega_z t \leqslant 2\pi, \end{cases}$$

$$\frac{\mu_{B,\mathbf{v}}^z(\Omega_z t)}{\Omega_z} = \begin{cases} 2g_1 v_z + 2g_1^{SL}, & 0 < \Omega_z t \leqslant \phi_1/2 \\ 2g_2 v_z + 2g_2^{SL}, & \phi_1 < \Omega_z t \leqslant \phi_2/2 \\ 2g_3 v_z + 2g_3^{SL}, & \phi_2 < \Omega_z t \leqslant \pi/2 \\ -\mu_{B,\mathbf{v}}^z(\pi - \Omega_z t), & \pi/2 < \Omega_z t \leqslant \pi \\ -\mu_{B,\mathbf{v}}^z(2\pi - \Omega_z t), & \pi < \Omega_z t \leqslant 2\pi. \end{cases} \quad (19)$$
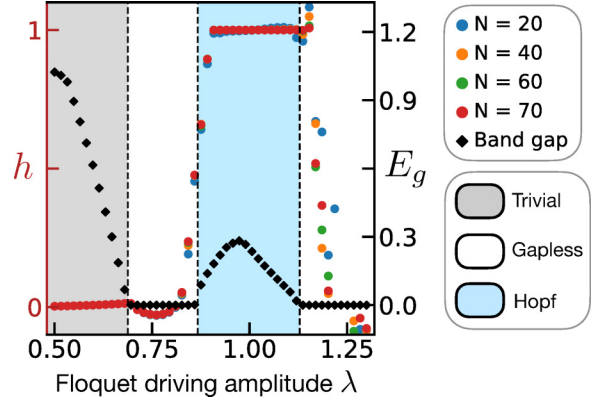

FIG. 4. Numerical evaluation of the Hopf invariant h for $N \times N \times N$ discretizations of momentum space (colored circles) and the band gap E_g (black diamonds; in units of the nearest-neighbor hopping t_{nn}) of the specified dipolar spin system as a function of the strength λ of the Floquet driving (defined in the main text), calculated with hopping range $R = 8$. The Hopf insulating phase (blue, right shaded) is observed across a range of λ; outside this range, the system transitions to gapless (white) and trivial insulating (gray, left shaded) phases.

Note that $\mu_{A,\mathbf{v}}^z(\Omega_z t)$ is even about π, guaranteeing that damping coefficients are real valued [see Eq. (12)]. The parameters g_i, g_i^{SL} can be tuned to achieve the desired hopping truncation.

D. Combining the two modulations

We now show that both of the above schemes can be implemented simultaneously, by choosing the frequencies of each to be well separated. Specifically, we take the modulation to be the sum of two components,

$$\mu_{\mathbf{r}}^\alpha(t) = \mu_{\mathbf{r}}^{xy,\alpha}(t) + \mu_{\mathbf{r}}^{z,\alpha}(t), \quad (20)$$

where $\mu_{\mathbf{r}}^{xy,\alpha}(t)$ is periodic with frequency Ω^{xy} and $\mu_{\mathbf{r}}^{z,\alpha}(t)$ with frequency Ω^z, and the frequencies satisfy either $\Omega^{xy} \gg \Omega^z$ or $\Omega^{xy} \ll \Omega^z$. Under this assumption, the dampings $\beta_{\mathbf{v}}^{\alpha\beta}$ factorize into a product of the two individual damping coefficients defined in Eqs. (16) and (18),

$$\beta_{\mathbf{v}}^{\alpha\beta} = \beta_{\mathbf{v}}^{xy,\alpha\beta}\beta_{\mathbf{v}}^{z,\alpha\beta}, \quad (21)$$

as desired. We verify that this assumption holds quantitatively in Fig. 6.

V. NUMERICAL VERIFICATION OF THE HOPF INSULATING PHASE

We now turn to a numerical exploration of the single-particle band structures supported in our dipolar Floquet system. By tuning the geometric and Floquet engineering parameters, we find transitions from topologically trivial band structures to the Hopf insulator and identify parameter regimes where the Hopf insulator's band gap can be as large as $E_g \gtrsim 0.26 t_{nn}$ (see Figs. 4 and 5). This occurs with a spacing $a = 0.99$ between adjacent planes of the same sublattice in the z direction (in units of the nearest-neighbor spacing in the xy plane), a spacing $b = 0.66$ between adjacent planes of the opposite sublattice, a staggered chemical potential
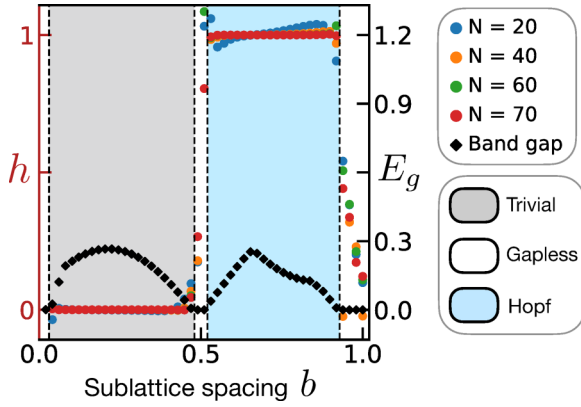
FIG. 5. Numerical evaluation of the Hopf invariant h for $N \times N \times N$ discretizations of momentum space (colored circles) and the band gap E_g (black diamonds; in units of the nearest-neighbor hopping t_{nn}) of the specified dipolar spin system as a function of the vertical spacing b between sublattices (in units of the nearest-neighbor spacing in the xy plane), calculated with hopping range $R = 8$. The Hopf insulating phase (blue, right shaded) is observed across a large range of b; outside this range, the system transitions to gapless (white) and trivial insulating (gray, left shaded) phases. Note that the Floquet modulation breaks the geometric symmetry $b \to 1 - b$, and hence the spectrum is not symmetric about $b = 0.5$.

$\mu^A - \mu^B = 2.28$ (in units of the nearest-neighbor hopping in the xy plane), and Floquet engineering parameters $g^{xy} = 1.2$, $g_{SL}^{xy} = 0.1$, $g_1 = -0.6$, $g_2 = 0.1$, $g_3 = 1.1$, $g_1^{SL} = 0.7$, $g_2^{SL} = -0.4$, $g_3^{SL} = 1.6$, $\phi_1 = 0.2$, $\phi_2 = 1.8$. These optimal parameters were found to optimize the Hopf insulating band gap via the basin-hopping optimization algorithm, a stochastic optimization algorithm that works well in rugged, high-dimensional optimization landscapes [71,72]. It consists of alternating steps of (i) performing local optimization to find a nearby local minima in the nearby energy landscape (i.e., the "basin"), and (ii) randomized "hopping" to more distant basins, whose local minima are then computed by repeating the first step. The Floquet engineering amplitudes are quite robust and can be varied together (replacing $g \to \lambda g$ for all amplitudes defined above) by $\sim 25\%$ about their optimal values while preserving Hopf insulating behavior (Fig. 4). The staggered chemical potential can be varied by $\sim 20\%$ [55]. Performing similar calculations for the lattice parameters, we find that the intrasublattice distance is also relatively robust and can be varied between 0.5 and 0.9 (Fig. 5), while the z-lattice spacing is slightly more sensitive, and should be kept within 0.92–1.08 in units of the x/y-lattice spacing (note that the most natural value of 1 lies well within this range).

We compute the momentum-space Bloch Hamiltonian by summing the Floquet engineered dipolar hoppings defined in Eqs. (4), (14), and (18). To truncate the infinite sum over the hopping distance, we only include hoppings to sites that are, at most, R unit cells away in each direction, i.e., $|r_\mu| \leqslant R$ for each $\mu = \{x, y, z\}$. The Hopf invariant is computed by evaluating the integral given by Eq. (2) on an $N \times N \times N$ grid in momentum space, solving $\nabla \times \mathbf{A}(\mathbf{k}) = \mathbf{j}(\mathbf{k})$ in the inverse Fourier domain to obtain the Berry connection [36]. The

computed invariant converges quickly to 1 as the discretization N becomes large, e.g., $h - 1 \approx 10^{-6}$ at $N = 70$, $R = 4$ (see, also, Figs. 5 and 4). We also see quick convergence of the band gap when increasing R, observing quantitative agreement within 10% for all $4 \leqslant R \leqslant 32$ and within 1% for all $8 \leqslant R \leqslant 32$.

VI. EDGE MODES OF THE DIPOLAR FLOQUET HOPF INSULATOR

In addition to its linking number invariant, the Hopf insulator's edge modes represent one of its key signatures and, crucially, one which can be experimentally probed. Up to now, these edge modes are only expected to appear at boundaries that are smooth at the scale of the lattice length, which act as a continuous variation of the two-band momentum-space Hamiltonian $H(\mathbf{k})$ across the boundary region. In this case, the Hopf insulator's nontrivial homotopy classification *requires* a gap closing in any edge between the Hopf insulator and the trivial insulator. Nevertheless, gapless edge modes have been observed numerically for "sharp" boundaries (i.e., open boundary conditions) [36] and, moreover, for the (001)-edge, were even shown to be robust to certain perturbations [39].

Meanwhile, recent work [44] has shown that the Hopf insulator's classification can be stabilized to higher bands by a certain crystalline symmetry,

$$JH(\mathbf{k})^* J^{-1} = -H(\mathbf{k}), \qquad (22)$$

where $JJ^* = -1$, although its classification is reduced to a $\mathbb{Z}_2$ invariant for band number greater than 2. This symmetry is, in fact, automatically satisfied in translationally invariant two-band systems (taking $J = \sigma_y$), and can generally be viewed as the composition of inversion and particle-hole symmetries.

Interestingly, we observe that—despite involving inversion symmetry—this crystalline symmetry is also obeyed at the *edge* of a two-band system, in the specific case of a sharp boundary (open boundary conditions). To see this, note that open boundary conditions are equivalent to an infinite δ function potential barrier at the edge of the system, $H_{edge} = \rho\sigma_z\delta_z$, $\rho \to \infty$, where σ_z acts on the sublattice degrees of freedom. In momentum space, this potential induces real all-to-all couplings between different values of k_z, $H_{edge}^{\mathbf{k},\mathbf{k}'} = \rho\sigma_z\delta_{k_x,k_x'}\delta_{k_y,k_y'}$. This is now easily seen to obey Eq. (22) with $J = \sigma_y$.

This observation suggests that the edge modes previously observed at sharp boundaries of the Hopf insulator are, in fact, protected by this "unintentional" crystalline symmetry, and are therefore not robust to perturbations that break the symmetry. To test this, we solve for the (100)-edge modes of the dipolar Hopf insulator via exact diagonalization for three different edge terminations: sharp, sharp with a symmetry-breaking perturbation, and adiabatic. We observe three qualitatively distinct spectra [Figs. 6(a)–6(c)]. The sharp edge hosts a linear energy degeneracy, consistent with previous studies [36,39]. To break the crystalline symmetry, we add a site-dependent chemical potential $\mu_{\mathbf{v}}\mathbb{1}$ localized on the two unit cells $\mathbf{v}$ nearest the edge. This perturbation gaps the edge mode, supporting our conjecture that the sharp edge modes of the Hopf insulator are, in fact, crystalline symmetry protected [73].
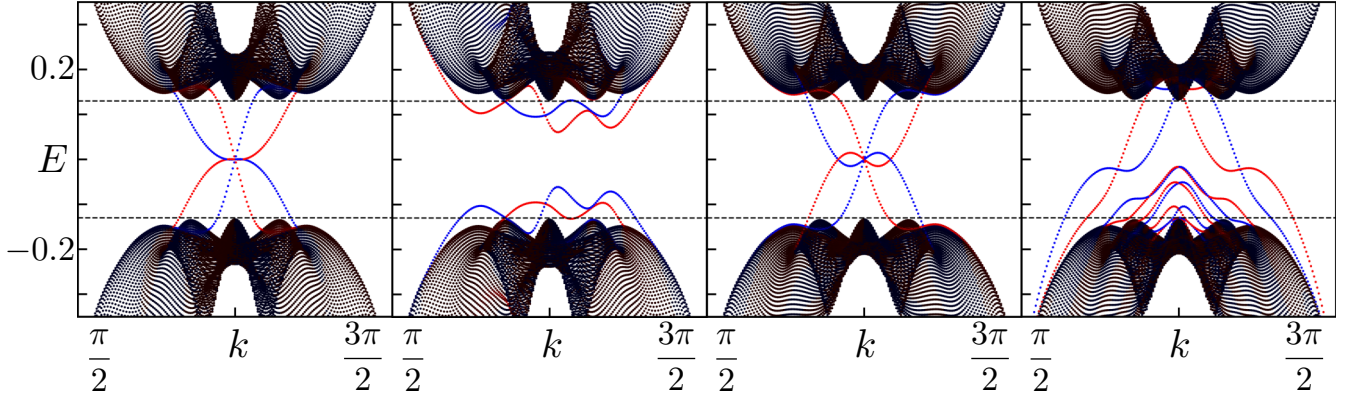
FIG. 6. Spectra for the (100)-edge of the Hopf insulator along the diagonal $k_y = k$, $k_z = \pi + k$, calculated from the effective Hamiltonian in Eq. (9). Color indicates a mode's mean x position, from red (light gray; localized at left edge), to black (bulk), to blue (dark gray; localized at right edge). Dashed lines mark the bulk band gap. A sharp edge (open boundary conditions) respects the symmetry given by Eq. (22) and leads to a gapless Dirac cone spectrum (far left). Adding a symmetry-breaking perturbation—in this case, a chemical potential on the two sites nearest the edge—gaps the Dirac cone (left center), demonstrating the nonadiabatic edge modes' lack of protection. In the adiabatic limit with edge termination smoothed over ~20 lattice sites, the edge spectrum is again gapless (right center). However, the Hopf invariant now protects the edge modes against *all* smooth perturbations to edge, including a smoothed bump in the chemical potential in the edge region (far right). For given transverse momenta k_y, k_z, the spectrum is calculated by first Fourier transforming the Hamiltonian along the y and z directions, and then performing exact diagonalization on the remaining 1D Hamiltonian. Sharp and smooth edge spectra are calculated for a lattice with 80 and 160 unit cells in the x direction, and hoppings are truncated at a range $R = 8$. As a check on the high-frequency approximation leading to the effective Hamiltonian given by Eq. (9), we also perform the same computation for the *exact* Floquet Hamiltonian, $H_F = i \ln\{\mathcal{T} \exp[-i \int_0^{2\pi/\Omega_{xy}} H(t)\, dt]\}$, at driving frequencies $\Omega_{xy} = 25\, t_{nn}$, $\Omega_z = 600\, t_{nn}$, and observe qualitatively identical edge spectra.

Finally, we consider smooth boundaries between the Hopf insulator and the trivial insulator. To construct smooth boundaries, we take the hoppings to be constant throughout the lattice, while an x-dependent staggered chemical potential $\mu_x \sigma_z$ tunes the Hamiltonian between the trivial phase at each end of the lattice and the Hopf insulating phase in the center. This interpolation occurs smoothly over two "edge regions" on either side of the Hopf insulating phase, consisting of ~20 lattice sites each. Shown in Fig. 6(c), these smooth edges also feature gapless edge modes. Importantly, the gaplessness of these edge modes is robust to *any* smooth perturbation to the lattice, including a "smoothed" version of the site-dependent chemical potential that was observed to gap the sharp edge mode [Fig. 6(d)].

VII. EXPERIMENTAL PROPOSAL

We now turn to our central result: a detailed blueprint for realizing the dipolar Hopf insulator using ultracold polar molecules. An explosion of recent experimental progress has led to the development of numerous possible molecular species [2–4,6,16], but for concreteness (and to demonstrate that the requisite separation of energy scales can be quantitatively realized), here we focus on ^{40}K ^{87}Rb [16,18–22].

We begin with the geometry and rotational level diagram illustrated in Fig. 1. The 3D optical lattice is generated using four pairs of counterpropagating beams, with two forming the xy lattice and two forming the A and B sublattices in the z direction. For experimental convenience, we envision the two sublattices to be formed by beams with orthogonal linear polarizations of light. In this case, a birefringent mirror can

control the relative phase between the two reflected beams, which in turn determines the separation between sublattices.

To realize the rotational level diagrams of Fig. 1, we first propose to tune the rotational states $|1, 0\rangle$ and $|1, 1\rangle$ of all molecules to be approximately degenerate using applied DC electric and magnetic fields, oriented in the z direction with amplitudes 1650 V/m and −490 G, respectively [74]. The degeneracy between the $|1, 0\rangle$ and $|1, 1\rangle$ states, and, in turn, the sublattice symmetry between the A and B planes, can then be broken by using *different* intensities of light to form each sublattice. Owing to the AC polarizability of ^{40}K ^{87}Rb, the lattice beams not only trap the molecules in the designated geometry, but also induce m_J-dependent shifts in the molecules' rotational states proportional to the beams' intensities [23]. The individual intensities, I_A and I_B, can therefore be tuned such that the transitions $|1, 0\rangle_A \leftrightarrow |0, 0\rangle_A$ and $|1, 1\rangle_B \leftrightarrow |0, 0\rangle_B$ are near resonant with each other, yet off resonant with all other transitions. Specifically, we calculate that x-polarized light with intensities $I_A = 0.43$ and $I_B = 0.54$ kW/cm^2 leads to the desired near resonance, with an energy gap $\delta \sim 5$ kHz to the nearest rotational state outside the prescribed doublets. Energy levels are calculated as in Ref. [23], and we assume that the x and y lattices are formed with z-polarized light of intensity 5 kW/cm^2. The molecule ^{40}K ^{87}Rb has a rotational splitting $\Delta = 2.2$ GHz and a measured dipolar interaction strength $t \sim 50$ Hz when trapped in a 3D optical lattice with 1064 nm light [21]. This scheme therefore naturally leads to the desired separation of energy scales, $t \ll \delta \ll \Delta$.

With the energy levels in hand, let us turn to the implementation of the Floquet modulations (Fig. 7). To realize the xy-plane modulation, we can again rely upon the AC polarizability, using a two-dimensional intensity-modulated
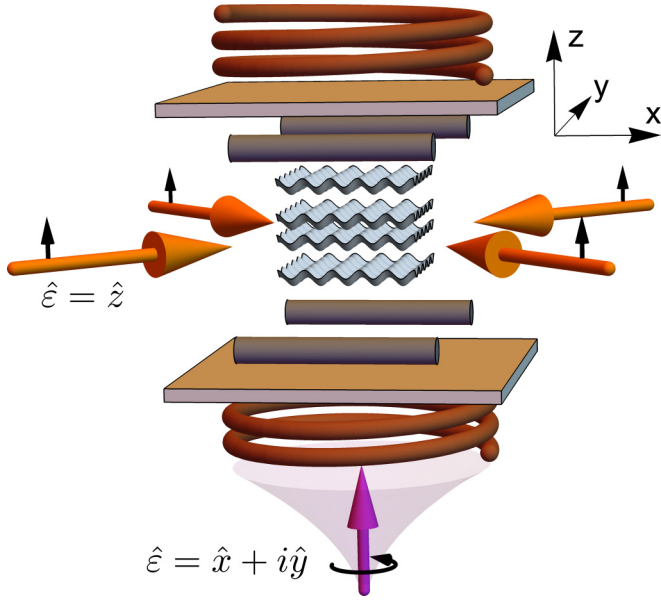
FIG. 7. Schematic of the proposed experiment, highlighting the mechanisms for Floquet modulation. The lattice (light-gray waves) is formed by three standing waves of laser light (beams not pictured). Stable electric field gradients are controlled by an electrode system of tungsten rods (dark-gray cylinders) and transparent plate electrodes (tan rectangles), while coils (brown spirals) generate a homogeneous magnetic field [75]. The xy-Floquet modulation is generated by z-polarized lasers forming a standing wave in the $(\hat{x} \pm \hat{y})$ directions (large orange arrows, left and right; polarization in small black arrows), using the AC polarizability of ^{40}K ^{87}Rb. The z-Floquet modulation is generated by a circularly polarized laser in the z direction (large purple arrow, bottom; polarization in small black arrow), which forms an intensity gradient along its direction of propagation due to the natural transverse spreading of a Gaussian laser beam.

standing wave to directly tune the molecules' energy levels nonuniformly in both space and time. The energy shifts of the $|1, 0\rangle_A$ and $|1, 1\rangle_B$ states can be made equal [necessary to ensure the modulation is of the form of Eq. (13)] by tuning the polar angle of the light's polarization to $\theta = 0.96$ rad, owing to the anisotropic polarizability of ^{40}K ^{87}Rb [23]. An additional stationary standing wave on the even sites can cancel the site-dependent nonzero average of the modulation, preserving translation invariance of the effective chemical potential. At a modulation frequency, $\Omega_{xy} \sim 500$ Hz, much greater than the dipolar interaction strength, $t_{nn} \sim 50$ Hz, the optimal modulation strength $g^{xy} = 1.2$ requires an intensity $\sim 10^{-2}$ kW/cm^2. An additional space-independent modulation of the two beams enables a difference between the two sublattices' modulations, achieving a nonzero g_{SL}^{xy}.

This method does not work for the z-gradient Floquet modulation, as a z gradient in the light's intensity is necessarily accompanied by a polarization in the orthogonal xy plane. In addition to shifting the molecules' energy levels, such a polarization would also induce mixing between rotational states, contaminating the desired hopping phase structure. Rather, we propose to achieve the z-gradient Floquet modulation by combining two independent sources of modulation [Figs. 8(c)–8(e)]. First, we apply an oscillating

electric field gradient of the order of $\delta E / \delta z \sim 1$ kV/cm^2. This gradient alone is not sufficient to realize the modulation of Eq. (13) because it shifts the energies of the the $|1, 0\rangle_A$ and $|1, 1\rangle_B$ states differently, owing to their different polarizability. We therefore combine this with a circularly polarized beam tuned *near*, but off, resonant with the $^3\Pi_{0^+}$ electronic excited state of ^{40}K ^{87}Rb, which shifts the energy levels of the low-lying rotation states of interest via the AC Stark shift [Figs. 8(a)–8(c)]. We imagine the beam to be traveling in the z direction, with the natural transverse spreading of the beam along its propagation axis giving rise to a z gradient in intensity $\delta I(z) / \delta z \sim I(z)/z$ [76]. To this end, we perform calculations of the AC polarizabilities of ^{40}K ^{87}Rb with circularly polarized light as a function of detuning from the $b^3\Pi_{0^+}$ state [Fig. 8(b)] using experimentally adjusted potential energy curves [77,78] as well as parallel and perpendicular electronic polarizabilities [23], which we expand on in detail in the following section. For σ^+ light, the polarizabilities have poles at the resonant transition frequency to the excited $J = 2$ state, which allows the corresponding energy shifts to be precisely controlled by the detuning over a large range. Modulating the detuning about resonance (as a step function, to avoid any resonance-induced decay) precisely realizes the desired Floquet modulation. Quantitatively, we find that detunings $\Delta\nu \sim 1$ GHz lead to AC polarizabilities $\alpha/h \sim$ 1 kHz/(W/cm^2), which in turn requires intensity gradients $\delta I/\delta z \sim 5$ W/(μm cm^2) to achieve the optimal Floquet parameters at modulation frequency $\Omega_z \sim 5$ kHz $\gg \Omega_{xy}$. At a distance $z \sim 100~\mu$m, the desired intensity gradient is thereby achieved with a modest intensity $I \sim 0.5$ kW/cm^2 and power $P \sim I(z) \times z^2 \sim 50$ mW [76].

We do not expect our proposed Floquet modulations to introduce substantial heating to the molecular system for a number of reasons. First, the modulations occur at a frequency that is significantly faster than the Hamiltonian energy scales, which exponentially suppresses many-body energy absorption [79]. Second, since the Hopf insulator's topology is characterized via its single-particle band structure, one only needs to excite a small number of molecules at any given time. At this single-particle level, the primary concern turns to heating from parametric processes associated with the laser intensity modulation. In this case, one can again utilize a separation of energy scales by choosing the frequencies of the Floquet modulation to be far removed from any trap resonances (i.e., the trap frequency and its harmonics) such that no parametric heating will take place [23,80]. Typical values of the trap frequency for ^{40}K ^{87}Rb experiments are ~ 20 kHz with a quality factor ~ 20 [80]; resonances are therefore easily avoided both in our simple order-of-magnitude estimate, $\Omega_z \sim 5$ kHz and $\Omega_{xy} \sim 500$ Hz, as well as our more quantitative estimate in Fig. 6, using $\Omega_z = 600 t_{nn} \approx 30$ kHz and $\Omega_{xy} = 25 t_{nn} \approx$ 1.25 kHz.

The edge modes of the dipolar Hopf insulator can be probed experimentally via molecular gas microscopy [81,82]. Here, a tightly focused beam applied near the edge induces local differences in the molecules' rotational splittings, enabling one to spectroscopically address and excite individual dipolar spins. The extent to which such an excitation remains localized on the edge during subsequent dynamics can be read
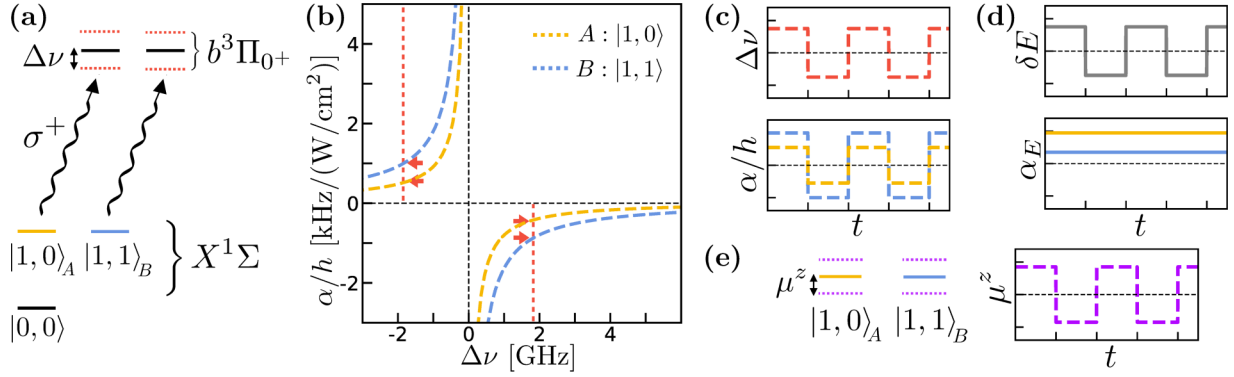
FIG. 8. Depiction of the two-component driving scheme used to implement the z-gradient Floquet modulation. (a) One component is realized using circularly polarized (σ^+) light tuned near, but off, resonant with the electronic transitions $|X^1\Sigma, v = 0, J = 1, m_J\rangle \rightarrow |b^3\Pi_{0^+}, v = 0, J = 2, m_J + 1\rangle$, with detuning $\Delta\nu$. Here, $X^1\Sigma, v = 0$ denotes the electronic ground-state manifold of the molecule, and $b^3\Pi_{0^+}, v = 0$ the relevant electronic excited-state manifold. This induces energy shifts in the electronic ground states of interest, $|1, 0\rangle_A$ and $|1, 1\rangle_B$, proportional to the AC polarizability α of ^{40}K ^{87}Rb at the particular detuning. (b) AC polarizabilities under circularly polarized σ^+ light as a function of the detuning $\Delta\nu$, calculated from first principles. Red dotted lines label two detunings that are oscillated between to achieve a step-function Floquet modulation. Red arrows indicate the corresponding polarizabilities. (c) Simplified depiction of the detuning and resulting polarizabilities as a function of time t. In the dipolar simulations, we use a higher parameter step function, given by Eq. (19), which allows greater flexibility to optimize the band gap of the Hopf insulating phase. The AC light intensity is held constant in time (not depicted). (d) The other component of modulation consists of an electric field gradient δE oscillated in time according to the same step function. The (DC) polarizabilities α_E of the $|1, 0\rangle_A$, $|1, 1\rangle_B$ states under this field are constant in time. (e) The polarizabilities and field amplitudes in (c) and (d) multiply to produce oscillating energy shifts μ^z (dotted purple) of the $|1, 0\rangle_A$, $|1, 1\rangle_B$ states. While each individual component of the z-gradient modulation produces a different magnitude shift for each state owing to the states' differing polarizabilities, the linear combination of both components can be chosen to produce equal shifts.

out using spin-resolved molecular gas microscopy. For polar molecules separated by a distance of 1 μm, single-molecule addressing of the $|0, 0\rangle \rightarrow |1, 0\rangle$ transition has been estimated to require a beam of radius 1 μm and a reasonable power of 10 μW [82]. The width of the edge region, typically large due to a wide harmonic confining potential, can be tuned via a number of recently developed techniques, including box potentials [83], additional "wall" potentials [84], or optical tweezers [85], allowing one to realize the three scenarios depicted in Fig. 6.

VIII. DETAILS OF AC POLARIZABILITIES FOR z-DIRECTION MODULATION

To effectively implement the Floquet modulation along the z direction, we use circularly polarized light tuned near a narrow transition, which allows light shifts to be precisely controlled by the detuning from the transition. Specifying to the molecule ^{40}K ^{87}Rb, we choose the dipole-forbidden transition $|X^1\Sigma^+, v = 0, J = 1, m_J\rangle \rightarrow |b^3\Pi_{0^+}, v = 0, J = 2, m_J + 1\rangle$ with 1028.7 nm [86] σ^+ light, where $m_J = 0$ for the A sublattice and 1 for the B sublattice. With relatively weak laser intensity (of the order of W/cm^2), the light shift can be characterized by the AC polarizability of the molecular state of interest. The polarizability is calculated from two different contributions. The first and more important contribution comes from the resonant transition, which has a strong dependence on the detuning, and the second contribution comes from all other transitions, that have a negligible dependence on the detuning in the range we are interested in. Here we assume the detuning is much larger than the spacings

between $|X^1\Sigma^+, v = 0, J = 1, m_J\rangle$ states with $m_J = 0$ and ± 1, and these spacings are much larger than the light shifts.

To characterize the contributions from the resonant transition, we follow the recipe in Refs. [87–89]. The generally complex dynamic polarizability for an alkali-metal molecule in a rovibrational state of the ground $X^1\Sigma^+$ potential is given by

$$\alpha(h\nu, \hat{\varepsilon})$$
$$= \frac{1}{\varepsilon_0 c} \sum_f \frac{E_f - E_i - ih\gamma_f/2}{(E_f - E_i - ih\gamma_f/2)^2 - (h\nu)^2} |\langle f|d\hat{R} \cdot \hat{\varepsilon}|i\rangle|^2,$$

$$(23)$$

where $\hat{\varepsilon}$ and ν are the polarization vector and the frequency of the light, respectively, c is the speed of light, ε_0 is the electric constant, $\hat{R}$ is the orientation of the interatomic axis, and d is the dipole operator. i denotes the rovibrational state $|i\rangle$ of interest with energy E_i in the ground $X^1\Sigma^+$ potential, and the summation over f denotes the summation over all rovibrational states $|f\rangle$ other than i with energies E_f in all electronic potentials, and γ_f describe the natural linewidths of $|f\rangle$.

When the laser frequency is very close to the narrow dipole-forbidden transition, the most significant contribution comes from that transition which has a pole at the resonant frequency and weakens as the inverse function of the detuning. We treat all transitions from $|X^1\Sigma^+, v = 0, J = 1, m_J\rangle$ to rovibrational states in the $b^3\Pi_{0^+}$ potential using Eq. (23). The largest contribution by far comes from the transition to the excited $v = 0$ state due to the similarity of its radial wave function to those in the ground potential. We use the

experimentally adjusted potential energy curves for both the excited $b^3\Pi_{0^+}$ state [77] and the ground $X^1\Sigma^+$ state [78], and a spin-orbit modified transition dipole moment between them [90]. Since the natural linewidths of the lowest rovibrational states in the $b^3\Pi_{0^+}$ potential are much smaller (of the order of kHz [86]) than the detunings that we are interested in (of the order of GHz), we take $\gamma_f = 0$.

The background contributions from all other transitions have negligible frequency dependence close to the 1028.7 nm transition due to the large detunings from the corresponding excited states. Thus we treat the background polarizabilities as constants throughout the detuning range. We use the method in Ref. [91] with experimentally determined electronic parallel and perpendicular polarizabilities [23] to calculate the background polarizabilities at 1064 nm and assume them to be the same near the 1028.7 nm transition. More specifically, we use $\alpha_{\parallel}/h = 10.0(3) \times 10^{-5}$ MHz/(W/cm^2) and $\alpha_{\perp}/h = 3.3(1) \times 10^{-5}$ MHz/(W/cm^2) determined for the wavelength of 1064 nm and obtain the background polarizabilities $\alpha_{bg,|1,0\rangle}/h = 4.64 \times 10^{-5}$ MHz/(W/cm^2) and $\alpha_{bg,|1,1\rangle}/h = 5.98 \times 10^{-5}$ MHz/(W/cm^2) for σ^+ polarization.

Finally, we add the two parts together to arrive at the total AC polarizabilities shown in Fig. 8(b).

IX. CONCLUSIONS

We have completed our specification of how Hopf insulating phases can be realized and detected in near-term experiments on ultracold polar molecules. As one of the few known topological insulators to fall outside both the traditional tenfold way classification as well as its extension to crystalline symmetries, the Hopf insulator is a particularly interesting phase of matter with many open questions eager for experimental input. For instance, we have proposed using the presence of a gapless edge mode at a smooth boundary, probed by spectroscopy, as a robust experimental diagnostic of the Hopf insulating phase. Recent work suggests that at the (001)-edge, this mode should feature a nonzero Chern number associated with an unusual bulk-to-boundary flow of Berry curvature [46]; numerous techniques to measure the Chern number have been developed [53,92–94], which may allow one to detect this physics. Looking to the future, an experimental Hopf insulator would be a vital resource in the search for a bulk response characterized by the Hopf invariant (analogous to the Hall effect in a Chern insulator), which so far remains unknown.

Our blueprint may also provide a basis from which to realize various extensions of the Hopf insulator. In our proposal, we have already seen that polar molecules can realize certain crystalline-symmetry-protected extensions of the Hopf insulator [44,46], which can be detected independently from the ordinary (noncrystalline) Hopf insulator by looking at sharp edge terminations that respect the crystalline symmetry. Polar molecules might also be used to realize driven extensions of the Hopf insulator, for instance, the Floquet Hopf insulator [47]. Here, one subjects the system to periodic driving at a timescale *comparable* to the hopping time, which can lead to a new Floquet Hopf insulating phase, characterized by a $\mathbb{Z} \times \mathbb{Z}_2$ pair of topological invariants that underlie an even richer spectrum of edge mode behavior than in the nondriven case. The Floquet Hopf insulator can be realized by strobing a flat band static Hopf insulator with periodic $\pi/2$ pulses of a staggered chemical potential [47]—the latter would be easily realized via a $\sim$100 Hz oscillation of the lattice light intensity. Realizing a sufficiently flat band Hopf insulator is a less trivial task, but the bandwidth could be optimized via standard optimization techniques depending on the specific set of available experimental parameters. More speculatively, a flat band Hopf insulator might also be a natural launching ground into many-body generalizations of the Hopf phase (much as a flat band Chern insulator is a key ingredient for the fractional Chern insulator [95]).

In the context of polar molecules, our work applies a number of tools developed for controlling and cooling polar molecules towards quantum simulation. We hope that some selection of these tools may find broader utility. For instance, our use of a sublattice-dependent lattice light intensity to realize (pseudo)spin-orbit coupling via the $\Delta m = 1$ component of the dipolar interaction may prove fruitful in realizing other topological phases as well. As a simple example to demonstrate wider applicability, the exact same form of spin-orbit coupling ($t_{\mathbf{r}}^{AB} \sim e^{i\phi}$) in 2D gives rise to Chern insulating physics [67]. In polar molecule setups limited by the ability to fill only a (random) fraction of the full set of lattice sites, the Chern insulator might therefore provide a disorder-robust [68] stepping stone to realizing the Hopf insulator. We have also provided implementations of two independent Floquet engineering schemes: an even-odd patterning utilizing the molecules' AC polarizability under lattice light, and a truncation of the power-law dipolar interaction in the z direction via a single circularly polarized Gaussian laser beam. Floquet engineering has proven critical in other quantum simulation platforms, and these techniques may serve as building blocks for its use in polar molecules. At a higher level, our work provides yet another piece of evidence for the power of dipolar interaction, and the potential of polar molecules as a quantum simulation platform.

[1] J. M. Sage, S. Sainis, T. Bergeman, and D. DeMille, Phys. Rev. Lett. **94**, 203001 (2005).

[2] J. W. Park, S. A. Will, and M. W. Zwierlein, Phys. Rev. Lett. **114**, 205302 (2015).

[3] T. Takekoshi, L. Reichsöllner, A. Schindewolf, J. M. Hutson, C. R. Le Sueur, O. Dulieu, F. Ferlaino, R. Grimm, and H.-C. Nägerl, Phys. Rev. Lett. **113**, 205301 (2014).

[4] M. Guo, B. Zhu, B. Lu, X. Ye, F. Wang, R. Vexiau, N. Bouloufa-Maafa, G. Quéméner, O. Dulieu, and D. Wang, Phys. Rev. Lett. **116**, 205303 (2016).

[5] A. Ciamei, J. Szczepkowski, A. Bayerle, V. Barbé, L. Reichsöllner, S. M. Tzanova, C.-C. Chen, B. Pasquiou, A. Grochola, P. Kowalczyk *et al.*, Phys. Chem. Chem. Phys. **20**, 26221 (2018).

[6] P. K. Molony, P. D. Gregory, Z. Ji, B. Lu, M. P. Köppinger, C. R. Le Sueur, C. L. Blackley, J. M. Hutson, and S. L. Cornish, Phys. Rev. Lett. **113**, 255301 (2014).

[7] S.-K. Tung, C. Parker, J. Johansen, C. Chin, Y. Wang, and P. S. Julienne, Phys. Rev. A **87**, 010702(R) (2013).

[8] J. Deiglmayr, A. Grochola, M. Repp, O. Dulieu, R. Wester, and M. Weidemüller, Phys. Rev. A **82**, 032503 (2010).

[9] M. G. Kozlov and L. N. Labzowsky, J. Phys. B: At., Mol. Opt. Phys. **28**, 1933 (1995).

[10] E. R. Hudson, H. J. Lewandowski, B. C. Sawyer, and J. Ye, Phys. Rev. Lett. **96**, 143004 (2006).

[11] J. Baron, W. C. Campbell, D. DeMille, J. M. Doyle, G. Gabrielse, Y. V. Gurevich, P. W. Hess, N. R. Hutzler, E. Kirilov, I. Kozyrev *et al.*, Science **343**, 269 (2014).

[12] M. S. Safronova, D. Budker, D. DeMille, Derek F. Jackson Kimball, A. Derevianko, and C. W. Clark, Rev. Mod. Phys. **90**, 025008 (2018).

[13] N. Balakrishnan, J. Chem. Phys. **145**, 150901 (2016).

[14] K.-K. Ni, T. Rosenband, and D. D. Grimes, Chem. Sci. **9**, 6830 (2018).

[15] R. Sawant, J. A. Blackmore, P. D. Gregory, J. Mur-Petit, D. Jaksch, J. Aldegunde, J. M. Hutson, M. Tarbutt, and S. L. Cornish, New J. Phys. **22**, 013027 (2020).

[16] K.-K. Ni, S. Ospelkaus, M. De Miranda, A. Pe'Er, B. Neyenhuis, J. Zirbel, S. Kotochigova, P. Julienne, D. Jin, and J. Ye, Science **322**, 231 (2008).

[17] S. A. Moses, J. P. Covey, M. T. Miecnikowski, D. S. Jin, and J. Ye, Nat. Phys. **13**, 13 (2017).

[18] J. Aldegunde, B. A. Rivington, P. S. Żuchowski, and J. M. Hutson, Phys. Rev. A **78**, 033434 (2008).

[19] J. Aldegunde, H. Ran, and J. M. Hutson, Phys. Rev. A **80**, 043410 (2009).

[20] S. Ospelkaus, K.-K. Ni, G. Quéméner, B. Neyenhuis, D. Wang, M. H. G. de Miranda, J. L. Bohn, J. Ye, and D. S. Jin, Phys. Rev. Lett. **104**, 030402 (2010).

[21] B. Yan, S. A. Moses, B. Gadway, J. P. Covey, K. R. A. Hazzard, A. M. Rey, D. S. Jin, and J. Ye, Nature (London) **501**, 521 (2013).

[22] S. A. Moses, J. P. Covey, M. T. Miecnikowski, B. Yan, B. Gadway, J. Ye, and D. S. Jin, Science **350**, 659 (2015).

[23] B. Neyenhuis, B. Yan, S. A. Moses, J. P. Covey, A. Chotia, A. Petrov, S. Kotochigova, J. Ye, and D. S. Jin, Phys. Rev. Lett. **109**, 230403 (2012).

[24] L. De Marco, G. Valtolina, K. Matsuda, W. G. Tobias, J. P. Covey, and J. Ye, Science **363**, 853 (2019).

[25] L. Anderegg, L. W. Cheuk, Y. Bao, S. Burchesky, W. Ketterle, K.-K. Ni, and J. M. Doyle, Science **365**, 1156 (2019).

[26] K. R. A. Hazzard, S. R. Manmana, M. Foss-Feig, and A. M. Rey, Phys. Rev. Lett. **110**, 075301 (2013).

[27] A. V. Gorshkov, K. R. Hazzard, and A. M. Rey, Mol. Phys. **111**, 1908 (2013).

[28] N. Y. Yao, M. P. Zaletel, D. M. Stamper-Kurn, and A. Vishwanath, Nat. Phys. **14**, 405 (2018).

[29] S. V. Syzranov, M. L. Wall, B. Zhu, V. Gurarie, and A. M. Rey, Nat. Commun. **7**, 13543 (2016).

[30] N. Y. Yao, A. V. Gorshkov, C. R. Laumann, A. M. Läuchli, J. Ye, and M. D. Lukin, Phys. Rev. Lett. **110**, 185302 (2013).

[31] M. Bukov, L. D'Alessio, and A. Polkovnikov, Adv. Phys. **64**, 139 (2015).

[32] T. E. Lee, Phys. Rev. A **94**, 040701(R) (2016).

[33] A. Micheli, G. Pupillo, H. P. Büchler, and P. Zoller, Phys. Rev. A **76**, 043604 (2007).

[34] C. H. Lee, W. W. Ho, B. Yang, J. Gong, and Z. Papić, Phys. Rev. Lett. **121**, 237401 (2018).

[35] H. Hopf, Math. Ann. **104**, 637 (1931).

[36] J. E. Moore, Y. Ran, and X.-G. Wen, Phys. Rev. Lett. **101**, 186805 (2008).

[37] A. P. Schnyder, S. Ryu, A. Furusaki, and A. W. W. Ludwig, Phys. Rev. B **78**, 195125 (2008).

[38] A. Kitaev, in *Advances in Theoretical Physics: Landau Memorial Conference*, edited by V. Lebedev and M. Feigelman, AIP Conf. Proc. No. 1134 (AIP, New York, 2009), p. 22.

[39] D.-L. Deng, S.-T. Wang, C. Shen, and L.-M. Duan, Phys. Rev. B **88**, 201105(R) (2013).

[40] D.-L. Deng, S.-T. Wang, and L.-M. Duan, Phys. Rev. B **89**, 075126 (2014).

[41] D.-L. Deng, S.-T. Wang, K. Sun, and L.-M. Duan, Chin. Phys. Lett. **35**, 013701 (2018).

[42] R. Kennedy and C. Guggenheim, Phys. Rev. B **91**, 245148 (2015).

[43] R. Kennedy, Phys. Rev. B **94**, 035137 (2016).

[44] C. Liu, F. Vafa, and C. Xu, Phys. Rev. B **95**, 161116(R) (2017).

[45] X.-X. Yuan, L. He, S.-T. Wang, D.-L. Deng, F. Wang, W.-Q. Lian, X. Wang, C.-H. Zhang, H.-L. Zhang, X.-Y. Chang *et al.*, Chin. Phys. Lett. **34**, 060302 (2017).

[46] A. Alexandradinata, A. Nelson, and A. A. Soluyanov, Phys. Rev. B **103**, 045107 (2021).

[47] T. Schuster, S. Gazit, J. E. Moore, and N. Y. Yao, Phys. Rev. Lett. **123**, 266803 (2019).

[48] Y. He and C.-C. Chien, Phys. Rev. B **99**, 075120 (2019).

[49] Y. He and C.-C. Chien, Phys. Rev. B **102**, 035101 (2020).

[50] H. Hu, C. Yang, and E. Zhao, Phys. Rev. B **101**, 155131 (2020).

[51] P. J. Ackerman and I. I. Smalyukh, Nat. Mater. **16**, 426 (2017).

[52] C. Wang, P. Zhang, X. Chen, J. Yu, and H. Zhai, Phys. Rev. Lett. **118**, 185701 (2017).

[53] M. Tarnowski, F. N. Ünal, N. Fläschner, B. S. Rem, A. Eckardt, K. Sengstock, and C. Weitenberg, Nat. Commun. **10**, 1728 (2019).

[54] Z. Yan, R. Bi, H. Shen, L. Lu, S.-C. Zhang, and Z. Wang, Phys. Rev. B **96**, 041103(R) (2017).

[55] T. Schuster, F. Flicker, M. Li, S. Kotochigova, J. E. Moore, J. Ye, and N. Y. Yao, Phys. Rev. Lett. **127**, 015301 (2021).

[56] D. Peter, N. Y. Yao, N. Lang, S. D. Huber, M. D. Lukin, and H. P. Büchler, Phys. Rev. A **91**, 053617 (2015).

[57] D. J. Thouless, M. Kohmoto, M. P. Nightingale, and M. den Nijs, Phys. Rev. Lett. **49**, 405 (1982).

[58] F. D. M. Haldane, Phys. Rev. Lett. **61**, 2015 (1988).

[59] C. L. Kane and E. J. Mele, Phys. Rev. Lett. **95**, 146802 (2005).

[60] M. König, S. Wiedmann, C. Brüne, A. Roth, H. Buhmann, L. W. Molenkamp, X.-L. Qi, and S.-C. Zhang, Science **318**, 766 (2007).

[61] L. Fu, C. L. Kane, and E. J. Mele, Phys. Rev. Lett. **98**, 106803 (2007).

[62] J. E. Moore and L. Balents, Phys. Rev. B **75**, 121306(R) (2007).

[63] R. Roy, Phys. Rev. B **79**, 195322 (2009).

[64] H. Zhang, C.-X. Liu, X.-L. Qi, X. Dai, Z. Fang, and S.-C. Zhang, Nat. Phys. **5**, 438 (2009).

[65] L. Fu, Phys. Rev. Lett. **106**, 106802 (2011).

[66] F. Schindler, A. M. Cook, M. G. Vergniory, Z. Wang, S. S. Parkin, B. A. Bernevig, and T. Neupert, Sci. Adv. **4**, eaat0346 (2018).

[67] X.-L. Qi, Y.-S. Wu, and S.-C. Zhang, Phys. Rev. B **74**, 085308 (2006).

[68] A. Agarwala and V. B. Shenoy, Phys. Rev. Lett. **118**, 236402 (2017).

[69] In the presence of external fields, which slightly mix the rotational eigenstates, we use $|J, m_J\rangle$ to refer to the state adiabatically connected to the associated rotational eigenstate.

[70] J. M. Brown and A. Carrington, *Rotational Spectroscopy of Diatomic Molecules* (Cambridge University Press, Cambridge, 2003).

[71] D. J. Wales and J. P. Doye, J. Phys. Chem. A **101**, 5111 (1997).

[72] P. Virtanen, R. Gommers, T. E. Oliphant, M. Haberland, T. Reddy, D. Cournapeau, E. Burovski, P. Peterson, W. Weckesser, J. Bright, S. J. van der Walt, M. Brett, J. Wilson, K. J. Millman, N. Mayorov, A. R. J. Nelson, E. Jones, R. Kern, E. Larson, C. J. Carey *et al.*, Nat. Methods **17**, 261 (2020).

[73] We hypothesize that the robustness of the (001)-edge modes [39] is an artifact of a similar stabilizing crystalline symmetry, perhaps related to the discrete rotation symmetry $k_x \rightarrow k_y, k_y \rightarrow -k_x, n_x \rightarrow n_y, n_y \rightarrow -n_x$ of the studied model, but we do not study this here.

[74] The presence of the DC electric field mixes the $|0, 0\rangle$ and $|1, 0\rangle$ states, and gives rise to additional long-range density-density *interactions* in the hard-core boson model [30]. We may neglect these in our study of the single-particle physics of the Hopf insulator.

[75] J. P. Covey, *Enhanced Optical and Electric Manipulation of a Quantum Gas of KRb Molecules* (Springer, New York, 2018).

[76] A. Yariv, *Optical Electronics*, 4th ed., The Holt, Rinehart and Winston Series in Electrical Engineering (Saunders College Publishing, Fort Worth, TX, 1991).

[77] K. Alps, A. Kruzins, M. Tamanis, R. Ferber, E. A. Pazyuk, and A. V. Stolyarov, J. Chem. Phys. **144**, 144310 (2016).

[78] A. Pashov, O. Docenko, M. Tamanis, R. Ferber, H. Knöckel, and E. Tiemann, Phys. Rev. A **76**, 022511 (2007).

[79] D. A. Abanin, W. De Roeck, and F. Huveneers, Phys. Rev. Lett. **115**, 256803 (2015).

[80] B. Neyenhuis, Ultracold polar KRb molecules in optical lattices, Ph.D. thesis, University of Colorado at Boulder, 2012.

[81] G. E. Marti, R. B. Hutson, A. Goban, S. L. Campbell, N. Poli, and J. Ye, Phys. Rev. Lett. **120**, 103201 (2018).

[82] J. P. Covey, L. De Marco, Ó. L. Acevedo, A. M. Rey, and J. Ye, New J. Phys. **20**, 043031 (2018).

[83] A. L. Gaunt, T. F. Schmidutz, I. Gotlibovych, R. P. Smith, and Z. Hadzibabic, Phys. Rev. Lett. **110**, 200406 (2013).

[84] P. Zupancic, P. M. Preiss, R. Ma, A. Lukin, M. E. Tai, M. Rispoli, R. Islam, and M. Greiner, Opt. Express **24**, 13881 (2016).

[85] L. Liu, J. Hood, Y. Yu, J. Zhang, N. Hutzler, T. Rosenband, and K.-K. Ni, Science **360**, 900 (2018).

[86] J. Kobayashi, K. Aikawa, K. Oasa, and S. Inouye, Phys. Rev. A **89**, 021401(R) (2014).

[87] S. Kotochigova and E. Tiesinga, Phys. Rev. A **73**, 041405(R) (2006).

[88] K. D. Bonin and V. V. Kresin, *Electric-Dipole Polarizabilities of Atoms, Molecules, and Clusters* (World Scientific, Singapore, 1997).

[89] A. J. Stone, *The Theory of Intermolecular Forces* (Clarendon, London, 1996).

[90] S. Kotochigova, E. Tiesinga, and P. S. Julienne, Eur. Phys. J. D **31**, 189 (2004).

[91] S. Kotochigova and D. DeMille, Phys. Rev. A **82**, 063421 (2010).

[92] H. M. Price and N. R. Cooper, Phys. Rev. A **85**, 033620 (2012).

[93] M. Aidelsburger, M. Lohse, C. Schweizer, M. Atala, J. T. Barreiro, S. Nascimbène, N. Cooper, I. Bloch, and N. Goldman, Nat. Phys. **11**, 162 (2015).

[94] M. Wimmer, H. M. Price, I. Carusotto, and U. Peschel, Nat. Phys. **13**, 545 (2017).

[95] E. J. Bergholtz and Z. Liu, Int. J. Mod. Phys. B **27**, 1330017 (2013).